An energy-based model for ferroelectric ceramics

Chaimae Babori, Mahmoud Barati, Laurent Daniel

European Journal of Mechanics / A Solids 103 (2024) 105151

Contents lists available at ScienceDirect

European Journal of Mechanics / A Solids

journal homepage: www.elsevier.com/locate/ejmsol

An energy-based model for ferroelectric ceramics

Chaimae Babori [a,b,*], Mahmoud Barati [a,b,c], Laurent Daniel [a,b]

[a] Université Paris-Saclay, CentraleSupélec, CNRS, Laboratoire de Génie Electrique et Electronique de Paris, 91192, Gif-sur-Yvette, France
[b] Sorbonne Université, CNRS, Laboratoire de Génie Electrique et Electronique de Paris, 75252, Paris, France
[c] Institut Polytechnique des Sciences Avancées, IPSA, 63 Boulevard de Brandebourg, 94200, Ivry-sur-Seine, France

ARTICLE INFO

Keywords:
Ferroelectricity
Energy-based modelling
Minor loop
Hysteresis
Dissipated energy

ABSTRACT

From the basic physical insight, the configuration and switching process of ferroelectric domains are both governed by energetic principles. Based on these energetic principles, a model for the nonlinear hysteretic behaviour of ferroelectric ceramics is developed. It relies on an energy-consistent thermodynamic formulation, based on two constitutive functions: free energy and dissipation. The model is grounded on an energy balance where the free energy and dissipation are known at all times during the polarisation process due to the incremental formulation obtained. All internal variables arise from the minimisation of a thermodynamic potential. Experimental measurements are performed in order to identify the parameters of the model and to validate the evolution of internal parameters generated by the energy-based model for different cases of loading. It is notably shown that the model allows capturing the energy losses under varying electrical loadings, which can be a key to the prediction of functional fatigue.

1. Introduction

Active materials play an essential role in intelligent systems design. Ferroelectrics are a popular category of active materials. They are widely used in various applications such as MEMS devices, medical imaging devices, ultrasonic transducers, sensors, and actuators (Booth and Goldsmith, 2017; Damjanovic, 2001; Granzow et al., 2021; Kimura et al., 2010; Mahbub et al., 2017; Smith, 2005). The coupled electro-mechanical behaviour of these materials is an essential aspect of their use in smart systems. Usually, the ferroelectric ceramics exploited in applications have a polycrystalline structure, formed of grains with different crystallographic orientations. Each grain is itself divided into domains with uniform spontaneous polarisation and strain (Fig. 1).

Ferroelectric ceramics exhibit a change in macroscopic polarisation and strain when subjected to external loading. A seemingly linear behaviour under low electro-mechanical loadings is observed, while the application of more intense electromechanical loadings produces a nonlinear and dissipative behaviour (Pardo and Ricote, 2011) (Fig. 2). For an unpoled material, the average polarisation, over a representative volume element, is null.

The variation of polarisation and strain is generated by intrinsic effects in relation to elasticity, dielectricity and piezoelectricity (Damjanovic and Taylor, 1999; Zhang et al., 1994), as well as extrinsic effects in relation to ferroelectricity and ferroelasticity, which refers to the reorientation of spontaneous polarisation and strain, respectively (Kamlah, 2001; Lynch, 1996). Extrinsic effects are related to domain switching and domain wall motion. Changes in polarisation are generated by both 180° domain wall motion and non-180° wall motion whereas non-180° wall motion induces a variation in strain (Cao and Evans, 1993; Kamlah, 2001).

Major hysteresis loops describing the nonlinear behaviour of ferroelectrics provide many important characteristics. In the ferroelectric hysteresis (Electric displacement versus electric field), it allows to define the coercive field, dielectric constant and remnant and saturation polarisation (Fig. 2). In the longitudinal strain versus electric field loop, the piezoelectric coefficients as well as the maximum strain can be defined. These features are key to the functional applications of ferroelectrics. In most applications, operating in a linear regime around remnant polarisation point (P_r in Fig. 2) is the optimum case. However, this apparently linear regime includes significant nonlinearity mostly due to domain switching (Daniel et al., 2015) which explains the need for hysteresis models.

To exploit the material properties at their maximum, to control and optimise ferroelectric devices, it is necessary to develop accurate models that can describe the nonlinear behaviour of ferroelectrics. Currently, a multitude of modelling approaches are available. They can be divided

* Corresponding author. Université Paris-Saclay, CentraleSupélec, CNRS, Laboratoire de Génie Electrique et Electronique de Paris, 91192, Gif-sur-Yvette, France.
E-mail address: chaimae.babori@centralesupelec.fr (C. Babori).

https://doi.org/10.1016/j.euromechsol.2023.105151
Received 13 January 2023; Received in revised form 19 August 2023; Accepted 26 September 2023
Available online 1 October 2023

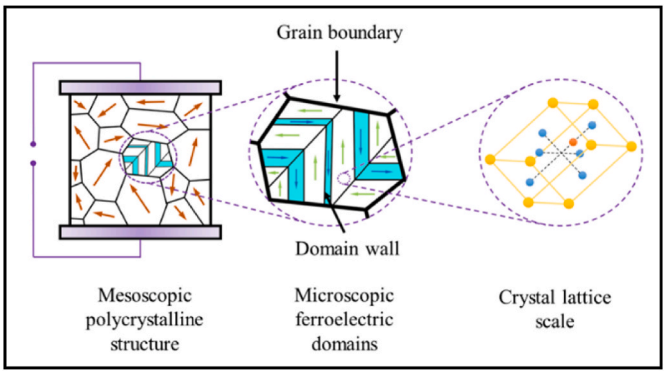

Fig. 1. Different scales for ferroelectric ceramics (Li et al., 2005).

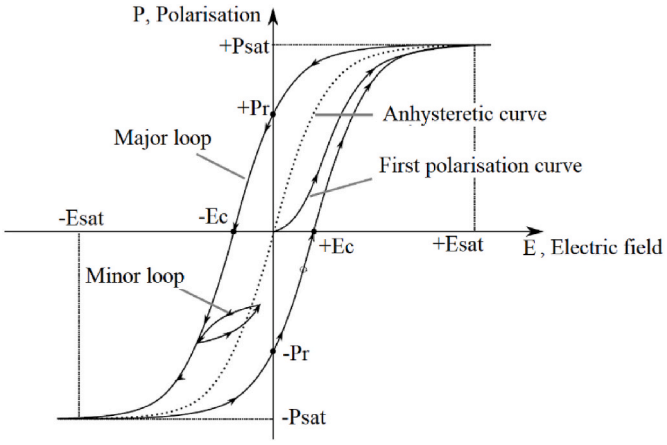

Fig. 2. Typical ferroelectric hysteresis curve.

into two main categories. One gathers macroscopic phenomenological models, and the other micro-electromechanical ones.

In recent years, macroscopic modelling of ferroelectric behaviour was studied and fed into finite element codes. Most of these models were inspired by viscoplasticity concept (Guillon et al., 2004), using internal variables such as remnant polarisation and remnant strain. Although this type of models is able to describe the general features of ferroelectricity, only few works treated the behaviour of ferroelectrics for minor loops (Ricinschi and Okuyama, 2007; Wang et al., 2017) (Fig. 2), which is the usual operating condition of ferroelectrics.

Phenomenological models consist of describing the state of the materials using internal variables at a specific instant and the evolution of these internal variables is governed by kinetic equations (Bassiouny et al., 1988a; Bassiouny and Maugin, 1989a; Chen, 1980; Kamlah and Böhle, 2001; Kamlah and Tsakmakis, 1999; Landis and McMeeking, 1999; Sateesh et al., 2008). The dependence of this modelling class on a large number of parameters may result in complex identification procedures. Moreover, the uniqueness of the material parameters may not be guaranteed due to the possible non-convexity of the underlying optimization problem related to their identification.

Bassiouny and his coworkers proposed phenomenological models based on the elastoplastic theory in the framework of continuum thermodynamics. In their works (Bassiouny et al., 1988a, 1988b; Bassiouny and Maugin, 1989a, 1989b), based on Helmoltz free energy, they used residual polarisation as internal variable to describe the behaviour of ferroelectrics under a multiaxial electromechanical loading. The choice of switching criterion and energy were developed later by (Cocks et al., 1999) and McMeeking for one-dimensional case of loading and extended to the multi-dimensional case in McMeeking and Landis works (Landis, 2002; McMeeking and Landis, 2002). In the former work (McMeeking and Landis, 2002), the only internal variable considered is the polarisation. In the latter work (Landis, 2002), the two internal variables, polarisation and strain were considered despite being governed by the same switching function.

(Schröder and Romanowski, 2005) proposed a fully electromechanically coupled formulation to model the dielectric and strain hysteresis. One switching function was defined to obtain the remnant polarisation. The remnant strain is assumed proportional to the deviatoric part of the dyadic product of polarisation. Another approach was introduced by (Kamlah, 2001; Kamlah and Tsakmakis, 1999). The internal variables were determined by a set of different switching criteria and saturation conditions that are based on the kinematic hardening plasticity theory.

Among all the proposed models to describe the ferroelectric behaviour, only few energy-based (EB) models were developed (Arockiarajan et al., 2010; Guillon et al., 2004; Jacques, 2018; Meindlhumer et al., 2021; Pechstein et al., 2021; Sands and Guz, 2013; Miehe et al., 2011) developed a continuum-based model exhibiting electro-magneto-mechanical coupling. In this work, a distinction was made between energy-based models and enthalpy-based. The energy-based models are considering that polarisation and strain are the independent control variables, whereas, for enthalpy-based models, the chosen independent control variables are the electric field and stress. (Sands and Guz, 2013) presented also a one-dimensional, rate independent model for piezoelectrics, based on the maximum entropy created. Another recent Energy-based model was developed by (Meindlhumer et al., 2021; Pechstein et al., 2021, 2020). The polarisation of the ferroelectric ceramic was presented as a dissipative process. A minimisation condition was added and formulated as a variational inequality taking as parameter the dielectric displacement, strain and remnant polarisation.

The second category of modelling approaches is the micromechanical models (Daniel et al., 2014a, 2014b; Huber, 2005; Hwang et al., 1995; Lange and Ricoeur, 2015; Lobanov and Semenov, 2019; Su and Weng, 2006; Tan and Kochmann, 2017). This type of models is based on the behaviour of a single crystal, single domain, or a single lattice cell. This approach is mandatorily combined with homogenization techniques to describe the macroscopic behaviour of ferroelectrics. The accuracy of the model depends on the averaging scheme adopted as well as the description of the local behaviour.

(Hwang et al., 1995) developed a micromechanical model where the polarisation and strain for an individual grain were predicted from the applied stress and electric field through a Preisach hysteresis model. The condition of switching was defined by an energy criterion. The response of the specimen to the applied loadings is deduced by averaging the response of grains at different orientations. A non-linear constitutive model for ferroelectric polycrystals was also developed by (Huber et al., 1999) to describe the nonlinear switching phenomenon in ferroelectrics under a coupled electromechanical loading. Huber assumed that the switching occurs within each crystal, which cause a change in remnant strain, polarisation, and other properties. The switching is based on the crystal plasticity theory developed by (Hill, 1966) and is resisted by the dissipative motion of domain walls.

(Daniel et al., 2014b) developed an anhysteretic multiscale model where the relation between the crystallographic texture and the macroscopic properties were investigated. In this model, an energetic description of the equilibrium at the single crystal level in conjunction with a statistical estimation of the ferroelectric domain structure were taken into account. This model can be used to take into consideration the contribution of the crystalline elastic anisotropy to the macroscopic behaviour and to the internal stress distribution in ferroelectrics under electromechanical loading (Daniel et al., 2014a).

(Lange and Ricoeur, 2015) presented a micro-electromechanically motivated model, considering a discrete switching in the unit cells and a quasi-continuous evolution of the irreversible fields for domain walls. In this model, the interaction between grains is considered by using an

Table 1
NCE55/PIC153 piezoelectric and dielectric coefficients from datasheet.

Parameter	$d_{33}(\times 10^{-12}\mathrm{m/V})$	$d_{31}(\times 10^{-12}\mathrm{m/V})$	$\varepsilon_{33}/\varepsilon_0$
NCE55	670	−260	5000
PIC153	600	–	4200

averaging method to calculate the effective irreversible electrical or mechanical fields.

(Tan and Kochmann, 2017) presented a variational constitutive model for polycrystalline ferroelectric ceramics. It describes the electro-mechanically coupled performance under an externally applied electric field and stress. The model starts at a single domain scale then develops to a single crystal with multiple domains, and finally extends to a polycrystal description. More recently, (Lobanov and Semenov, 2019) proposed a micro-mechanical model where they added the phases effect. This model is able to describe the behaviour for tetragonal, rhombohedral, and orthorhombic phases.

Another micromechanical model is developed by (Arockiarajan et al., 2010) where the grain boundary effect is examined. The activation of domain switching process is described using Gibbs free energy. The main characteristic of the model is the integration of the effects of the stress imposed by surrounding grains on a switching grain.

The main objective of this study is to develop a model to predict the evolution of polarisation and strain for ferroelectrics under unipolar and bipolar loadings and to directly calculate the energy loss. The model presented in this paper is a thermodynamically consistent phenomenological model taking in consideration the spatial variation of properties, combining the two categories of models and inspired from the energy-based model for ferromagnetic materials (Da Silva et al., 2022; Jacques et al., 2018). The novelty of the proposed model stands in the ability to describe the nonlinear behaviour of ferroelectrics under low electric field around remanent polarisation and in the method adopted to define the free energy which is based on a multi-scale approach describing the volume fraction of ferroelectric domains (Daniel et al., 2014b), unlike the previously proposed energy-based models, where the free energy is defined phenomenologically. The polarisation is obtained by minimisation of a thermodynamic potential. To take into account the progressive nature of polarisation mechanisms, the model considers several cells characterized by different and varying coercive fields. The overall macroscopic strain and polarisation are obtained by averaging the response of all the cells considered.

The paper is divided into four major sections. The first section presents the studied materials and experimental setup. The second section is dedicated to the energy-based model, fundamental equations, constitutive laws, and a description of the variational approach adopted. The third section will be entirely devoted to the procedure of identification of the energy-based model parameters using experimental measurements. The final section is the validation of the model proposed for two different types of modified soft lead zirconate titanate. The capability of the proposed model to predict minor ferroelectric and ferroelastic loops as well as major loops is verified for both materials.

2. Experimental set-up and studied materials

The studied materials are both soft piezoelectric ceramics, commercially designed NCE55 and PIC 153 from Noliac and PI ceramic, respectively (Noliac; PI Ceramic. The dimension of the specimens is $4 \times 4 \times 4\ \mathrm{mm}^3$ and silver electrodes are provided on two opposite surfaces. The piezoelectric and dielectric coefficients, indicating respectively the ratio of strain with respect to the applied electric field and the permittivity of the material, are given in Table 1. d_{33} is the piezoelectric coefficient obtained from the longitudinal strain of the sample (Fig. 12), whereas d_{31} is calculated using the transversal strain values.

The bench test used for strain and dielectric displacement measurements is described in Fig. 3 (Segouin et al., 2019). The sample is placed between two fixtures, electrically isolated using Teflon parts and immersed in an insulating fluid (Fluorinert™ FC-770, 3 M) to prevent dielectric breakdown. The electric field E is produced by a high voltage amplifier (Trek 20/20C-HS) and controlled by a real time Dspace hardware module with a maximum sampling frequency of 5 kHz. The dielectric displacement D is measured from the upper electrode of the sample using an integrating capacitor of 2057nF (Glazer et al., 1984) and recorded using the same module.

During experiments, the strain field is measured by Digital Image Correlation (DIC) (Segouin et al., 2017). A random speckle pattern is painted on a lateral face to create a tracking texture. The procedure of preparation of the artificial texture is described in (Segouin et al., 2019, 2017). This face is imaged using a high-resolution camera (Ximea MD091MU-SY, 14 Monochrome, 3380 × 2708 px) with a maximum frame rate of 5 Hz mounted on a long-distance microscope (Questar QM100MKIII). The optical resolution of the system is ~5 μm. The sample is imaged through a flat glass window of 1mm of thickness. The whole optical system is placed at 38 cm from the sample surface. The lighting of the surface is ensured by a light source (LLS3 LED). The exposure time is fixed to 4 ms per image. The image acquisition by the camera is triggered using the same Dspace module that acquires the electric field E. The images record is then synchronized with the application of the loading. A MATLAB program allows to calibrate the positioning of the sample based on an image gradient analysis and is used to

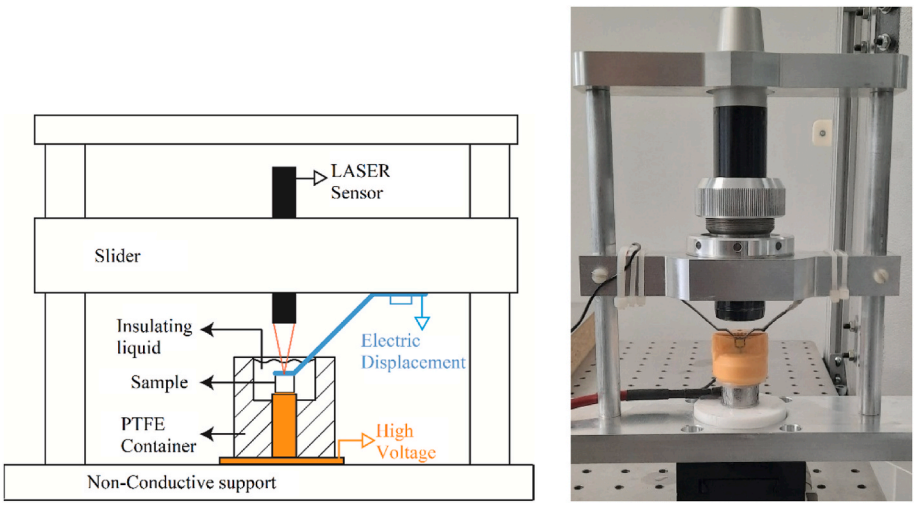

Fig. 3. schematic drawing and general view of the measurement bench.

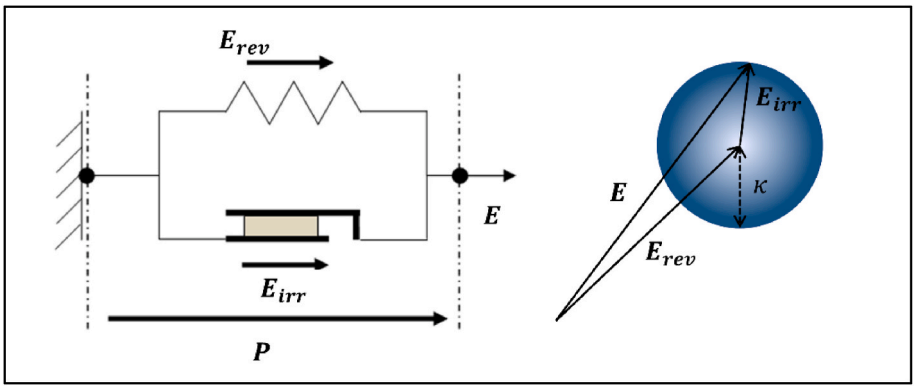

Fig. 4. Mechanical analogy of the energy-based model (Jacques et al., 2018).

process the images. The TIFF format of the recorded images are correlated using CorelliRT3 (Tomičević et al., 2013) which is a 2D-DIC MATLAB program. The strain field is then obtained from the displacement field.

The frequency of acquisition of DIC is related to the frequency of the applied loading. Although many images are needed to get accurate results, there is a limitation for the number of images that can be saved using DIC during the experiment. As a complementary measurement, a laser sensor (IFS 2405-1), connected to a controller (IFC 2471), is used to measure the longitudinal strain.

3. Energy-based model

In the energy-based hysteresis model developed in this article, the dielectric displacement and strain are taken as the primary unknowns, while the remnant polarisation is used as an internal variable. This choice of internal variables is not unique but was made in accordance with the multiscale approach (Daniel et al., 2014b) that is used as a basis for the anhysteretic response. The dissipation model is grounded on an analogy between pinning field and a dissipative dry friction force, inspired from an approach developed to model the behaviour of ferromagnetic materials (François-Lavet et al., 2013; Henrotte et al., 2006).

3.1. Single-cell approach

As shown in Fig. 4, the electric field is supposed to be analogous to the applied force and therefore the displacement corresponds to the polarisation. The applied electric field is decomposed into a reversible $\mathbf{E}_{\text{rev}}$ and irreversible part $\mathbf{E}_{\text{irr}}$. The reversible part acts like a spring force, while the irreversible part is similar to a dry friction force (Steentjes et al., 2014). The friction slider is activated once the norm of the applied electric field surpasses the pinning field threshold κ.

The hysteresis model is based on the conservation of energy (Bergqvist, 1997; Jacques, 2018). The first and second law of thermodynamics can be expressed through the Clausius-Duhem inequality:

$$\Delta = \mathbf{E}.\dot{\mathbf{P}} + \mathbf{T} : \dot{\boldsymbol{S}} - \dot{\psi} \geq 0 \tag{1}$$

where Δ is the dissipation, ψ is the Helmholtz free energy, $\mathbf{E}.\dot{\mathbf{P}}$ is the electric work and $\mathbf{T} : \dot{\boldsymbol{S}}$ is the mechanical work. The term $\mathbf{T} : \dot{\mathbf{S}}$ vanishes in the case of stress-free loading. ψ is chosen as an explicit function of the polarisation $\mathbf{P}$.

In the case of reversible transformation, the dissipation is null. Therefore, the rate $\dot{\psi}$ of the Helmholtz free energy is a function of the polarisation $\mathbf{P}$ and can be written as:

$$\dot{\psi} = \mathbf{E}_{\text{rev}}.\dot{\mathbf{P}} \text{ with } \mathbf{E}_{\text{rev}} = \frac{\partial \psi}{\partial \mathbf{P}} \tag{2}$$

$\mathbf{E}_{\text{rev}}$ is called reversible electric field. In the reversible context, the electric work is totally transformed into internal energy. Considering that the internal energy ψ is convex and smooth, $\mathbf{P}$ and $\mathbf{E}_{\text{rev}}$ are related by a one-to-one function that is said to be anhysteretic (see Fig. 5). This relation can be expressed by:

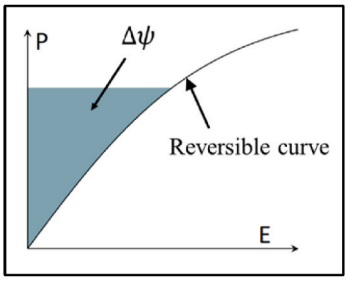

Fig. 5. Representation of the anhysteretic P-E curve and corresponding free energy.

$$\mathbf{P} = \mathbf{P}_{\text{an}}(\mathbf{E}_{\text{rev}}) \leftrightarrow \mathbf{E}_{\text{rev}} = \mathbf{P}_{\text{an}}^{-1}(\mathbf{P}) \tag{3}$$

$\mathbf{P}_{\text{an}}$ is a convenient notation for the reciprocal of the function $\frac{\partial \psi}{\partial \mathbf{P}}$ where $\psi = \psi(\mathbf{P})$.

The general expression of the dissipation is obtained using equations (1) and (2):

$$\Delta = (\mathbf{E} - \mathbf{E}_{\text{rev}}).\dot{\mathbf{P}} \geq 0 \tag{4}$$

In ferroelectrics, the nonlinear dissipative response results from domain wall movement characterized by pinning-depinning dynamics (Paruch and Guyonnet, 2013; Smith and Hom, 1999). It is known that the coercive field of ferroelectrics is related to the pinning-depinning transition of domain walls (Yang et al., 1999).

The dissipation depends on the variation of the internal variable (i.e., polarisation) and is assumed to be equal to the rate of a work caused by dry friction:

$$\Delta = \kappa|\dot{\mathbf{P}}| \tag{5}$$

κ is the pinning field amplitude and is a positive scalar for an isotropic material. It was shown that, in ferroelectric ceramics, not all the irreversible field dissipates upon mechanical loadings, and by comparing hysteresis loops and self-heating measurements, it was found that a part of the irreversible field contributes to some trapped energy (Barati et al., 2021). But here, for simplicity, it is assumed that all work associated with the irreversible field is dissipated. We can then express the dissipation in terms of the irreversible electric field $\mathbf{E}_{\text{irr}}$:

$$\Delta = \mathbf{E}_{\text{irr}}.\dot{\mathbf{P}} \tag{6}$$

We can deduce another expression of the equilibrium equation using equations (4) and (6) after factorisation of $\dot{\mathbf{P}}$:

$$(\mathbf{E}-\mathbf{E}_{\text{rev}}-\mathbf{E}_{\text{irr}}).\dot{\mathbf{P}}=0 \tag{7}$$

Equation (7) is not differentiable for $\dot{P}=0$. Since the functional is convex, we can define $\mathbf{E}_{\text{irr}}$ as a set of sub-gradients of the functional Δ in lieu of a single-valued gradient.

$$\mathbf{E}-\mathbf{E}_{\text{rev}}-\mathbf{E}_{\text{irr}}=\mathbf{0}\rightarrow\mathbf{E}-\frac{\partial\psi}{\partial\mathbf{P}}\in\partial\Delta(\dot{\mathbf{P}})=\begin{cases}\mathbf{E}_{\text{irr}},|\mathbf{E}_{\text{irr}}|\leq\kappa\ \text{if}\dot{\mathbf{P}}=0\\ \mathbf{E}_{\text{irr}}=\kappa\dfrac{\dot{\mathbf{P}}}{|\dot{\mathbf{P}}|}\ \text{otherwise}\end{cases} \tag{8}$$

Equation (8) is the fundamental equation of the energy-based hysteresis model for a single cell.

The single cell prediction for the major loop is in good agreement with experimental results, but the experiments have shown that it is less accurate for minor loops (Jacques, 2018; Jacques et al., 2018). To obtain more accuracy from the model, a set of different strengths of pinning fields can be used. Therefore, a multi-cell approach is adopted (Bergqvist, 1997; Henrotte et al., 2014) where the pinning field follows a distribution law (Bergqvist et al., 1997; Bertotti, 1998).

The pinning field strength for each cell is therefore considered as $\kappa^*(\lambda)=\lambda\kappa$. λ is a dimensionless value which characterizes each cell and scales the width of the hysteresis loop, with a given probability $\zeta(\lambda)$ that corresponds to the weight of the contribution of the cell λ. It is important to note that the notion of cells refers to the numerical implementation of the dissipation and is not explicitly connected to individual ferroelectric domains inside the material.

3.2. Multi-cell approach

The polarisation associated to each cell λ is denoted by $\mathbf{P}^*(\lambda)$. The density of the free energy stored in the λ-cell $\psi^*(\mathbf{P}^*(\lambda))$ is related to the free-energy by:

$$\psi^*(\mathbf{P}^*(\lambda))=\zeta(\lambda)\psi\left(\frac{\mathbf{P}^*(\lambda)}{\zeta(\lambda)}\right) \tag{9}$$

Such that $\dot{\psi}^*(P^*(\lambda))=\mathbf{E}^*_{\text{rev}}(\lambda).\dot{\mathbf{P}}^*(\lambda)$.

The dissipation in the λ-cell is expressed as follows:

$$\Delta^*(\lambda)=|\kappa^*(\lambda)\dot{\mathbf{P}}^*(\lambda)|=\mathbf{E}^*_{\text{irr}}(\lambda).\dot{\mathbf{P}}^*(\lambda) \tag{10}$$

Each λ-cell satisfies the fundamental equation of the energy-based model:

$$\mathbf{E}-\frac{\partial\psi^*}{\partial\mathbf{P}^*}\in\partial\Delta^*(\mathbf{P}^*(\lambda))=\begin{cases}\mathbf{E}^*_{\text{irr}}(\lambda),|\mathbf{E}^*_{\text{irr}}(\lambda)|\leq\kappa^*(\lambda),\text{if}\ \dot{\mathbf{P}}^*(\lambda)=0\\ \mathbf{E}^*_{\text{irr}}(\lambda)=\kappa^*(\lambda)\dfrac{\dot{\mathbf{P}}^*(\lambda)}{|\dot{\mathbf{P}}^*(\lambda)|},\text{otherwise}\end{cases} \tag{11}$$

In the multi-cell approach, we assume that λ-cells are independent. Equation (11) is satisfied for each cell.

The macroscopic polarisation is expressed as the sum of all λ-cell contribution:

$$\mathbf{P}=\int_0^\infty\mathbf{P}^*(\lambda)\mathrm{d}\lambda \tag{12}$$

Integration of equation (8) over each cell λ allows to get the homogenized energy balance:

$$\mathbf{E}.\dot{\mathbf{P}}=\int_0^\infty(\mathbf{E}^*_{\text{rev}}(\lambda).\dot{\mathbf{P}}^*(\lambda))\mathrm{d}\lambda+\int_0^\infty(\mathbf{E}^*_{\text{irr}}(\lambda).\dot{\mathbf{P}}^*(\lambda))\mathrm{d}\lambda \tag{13}$$

The energy-based equation for each cell after discretization becomes:

$$\mathbf{E}-\frac{\partial\psi}{\partial\mathbf{P}^{\mathbf{k}}}\in\partial\Delta^{\mathbf{k}}(\dot{\mathbf{P}}^{\mathbf{k}})=\begin{cases}\mathbf{E}^{\mathbf{k}}_{\text{irr}},|\mathbf{E}^{\mathbf{k}}_{\text{irr}}|\leq\kappa^{\mathbf{k}},\text{if}\ \dot{\mathbf{P}}^{\mathbf{k}}=0\\ \mathbf{E}^{\mathbf{k}}_{\text{irr}}=\kappa^{\mathbf{k}}\dfrac{\dot{\mathbf{P}}^{\mathbf{k}}}{|\dot{\mathbf{P}}^{\mathbf{k}}|},\text{otherwise}\end{cases} \tag{14}$$

The second step after establishing the energy-based model equations is the discretization of the pinning field distribution. λ is divided into N parts, each part is characterized by a specific weight $\omega^{\mathbf{k}}$ and a pinning field strength $\kappa^{\mathbf{k}}$, given by:

$$\omega^{\mathbf{k}}=\int_{\lambda^{k-1}}^{\lambda^{\mathbf{k}}}\zeta(\lambda)\mathrm{d}\lambda,\ \kappa^{\mathbf{k}}=\frac{\int_{\lambda^{k-1}}^{\lambda^{\mathbf{k}}}\zeta(\lambda)\kappa^*(\lambda)\mathrm{d}\lambda}{\omega^{\mathbf{k}}} \tag{15}$$

For the numerical implementation of the hysteresis model, the variational approach is adopted, which was investigated for ferromagnetic materials in (François-Lavet et al., 2013) and in ferroelectric materials in (Mielke and Timofte, 2006). It consists of searching an exact solution of the non-linear equation (14) by assigning a functional $\Omega^{\mathbf{k}}$ of the state variable $\mathbf{P}^{\mathbf{k}}$ to each cell. The polarisation can evolve only in the sense of minimisation of the functional $\Omega^{\mathbf{k}}$. The functional is defined in two steps: first, the Landau free energy, which is linked to Helmholtz potential by:

$$g^{\mathbf{k}}(\mathbf{E},\mathbf{P}^{\mathbf{k}})=\psi(\mathbf{P}^{\mathbf{k}})-\mathbf{E}.\mathbf{P}^{\mathbf{k}} \tag{16}$$

Such that:

$$\frac{\partial g^{\mathbf{k}}}{\partial\mathbf{P}^{\mathbf{k}}}=\frac{\partial\psi}{\partial\mathbf{P}^{\mathbf{k}}}-\mathbf{E} \tag{17}$$

Second, the dissipation $\Delta^{\mathbf{k}}$ is a function of $\dot{\mathbf{P}}^{\mathbf{k}}$, while the functional $\Omega^{\mathbf{k}}$ is assumed in term of $\mathbf{P}^{\mathbf{k}}$. A pseudo-potential is defined to solve this disagreement:

$$\widetilde{\Delta}^{\mathbf{k}}\left(\mathbf{P}^{\mathbf{k}},\mathbf{P}^{\mathbf{k}}_{(\mathbf{p})}\right)=\kappa^{\mathbf{k}}\left|\mathbf{P}^{\mathbf{k}}-\mathbf{P}^{\mathbf{k}}_{(\mathbf{p})}\right| \tag{18}$$

Whose sub-gradient:

$$\frac{\partial\widetilde{\Delta}^{\mathbf{k}}\left(\mathbf{P}^{\mathbf{k}},\mathbf{P}^{\mathbf{k}}_{(\mathbf{p})}\right)}{\partial\mathbf{P}^{\mathbf{k}}}=\begin{cases}\mathbf{E}^{\mathbf{k}}_{\text{irr}},\left|\mathbf{E}^{\mathbf{k}}_{\text{irr}}\right|\leq\kappa^{\mathbf{k}},\text{if}\ \ \mathbf{P}^{\mathbf{k}}=\mathbf{P}^{\mathbf{k}}_{(\mathbf{p})}\\ \mathbf{E}^{\mathbf{k}}_{\text{irr}}=\kappa^{\mathbf{k}}\dfrac{\mathbf{P}^{\mathbf{k}}-\mathbf{P}^{\mathbf{k}}_{(\mathbf{p})}}{\left|\mathbf{P}^{\mathbf{k}}-\mathbf{P}^{\mathbf{k}}_{(\mathbf{p})}\right|},\text{otherwise}\end{cases} \tag{19}$$

Using equations (17) and (18), equation (17) can be reformulated as:

$$\frac{\partial}{\partial\mathbf{P}^{\mathbf{k}}}\left(g^{\mathbf{k}}+\widetilde{\Delta}^{\mathbf{k}}\right)=0 \tag{20}$$

That results in the functional to be minimized:

$$\Omega^{\mathbf{k}}\left(\mathrm{E},\mathbf{P}^{\mathbf{k}},\mathbf{P}^{\mathbf{k}}_{(\mathbf{p})}\right)=g^{\mathbf{k}}\left(\mathrm{E},\mathbf{P}^{\mathbf{k}}\right)+\widetilde{\Delta}^{\mathbf{k}}\left(\mathbf{P}^{\mathbf{k}},\mathbf{P}^{\mathbf{k}}_{(\mathbf{p})}\right) \tag{21}$$

3.3. Helmholtz free energy

To minimize the functional $\Omega^{\mathbf{k}}$, we need to define the Helmholtz free energy. For this purpose, a simplification of the multi-scale model for reversible ferroelectric behaviour will be utilized (Daniel et al., 2014b). This model is based on the energy description of the equilibrium at a single crystal scale. Each single crystal is described as a set of domain families, each of them is associated to a particular easy axis. The free energy of each domain family is given by:

$$\psi_\alpha=-\mathbf{E}_\chi.\mathbf{P}_\alpha-\mathbf{T}_\chi:\mathbf{S}^{\text{fe}}_\alpha-2\mathbf{E}_\chi.\mathbf{d}^{\text{pz}}_\alpha:\mathbf{T}_\chi \tag{22}$$

ψ_α is the free energy of a domain family. $\mathbf{E}_\chi$, $\mathbf{T}_\chi$ are electric field and stress at the single crystal scale and $\mathbf{P}_\alpha$, $\mathbf{S}^{\text{fe}}_\alpha$, $\mathbf{d}^{\text{pz}}_\alpha$ are respectively the polarisation, strain, and piezoelectric coefficient at the ferroelectric domain scale. The simplified multiscale model (SMSM) requires the identification of the following parameters:

- Dielectric permittivity ε, assumed isotropic (so that ε is a scalar): its value was taken from (Kamlah and Wang, 2003), for a similar material.

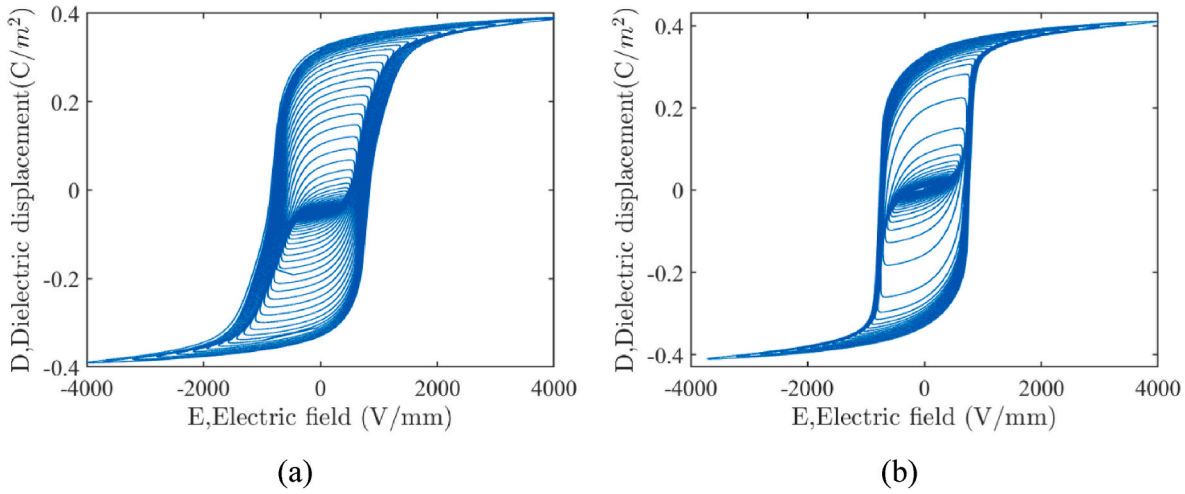

Fig. 6. Hysteresis loop using 48 amplitudes for (a) NCE55 and (b) PIC153.

- Spontaneous polarisation P_0 of the single crystal: its value was taken as $1.2 \times P_s$, following the homogenization rule found in (Li and Rajapakse, 2007) (it is 1.20 for tetragonal and 1.16 for rhombohedral ceramics). P_s is the macroscopic saturation polarisation of the material, identified from macroscopic measurements (see later in the text).
- Adjustment parameter A_S: this parameter is shown in (Daniel et al., 2014b) to be proportional to the initial slope χ^0 of the anhysteretic polarisation curve ($A_s = \frac{3\chi^0}{P_0^2}$). In practice χ^0 was taken as the maximum susceptibility extracted from the experimental major P-E loop.

Other parameters are needed for the SMSM (piezoelectric coefficients d_{33}, d_{13}, d_{15} for the single crystal and spontaneous polarisation strain λ_0) but do not play any role in the case of stress-free polarisation curves.

The expression of the free energy ψ obtained from the SMSM is fitted into a scalar saturation curve depending on the polarisation only (the strain contribution is omitted):

$$\psi(P) = A \times P_s \left(\frac{P}{P_s} \operatorname{atanh}\left(\frac{P}{P_s}\right) + \frac{1}{2} \ln \left| \left(\frac{P}{P_s}\right)^2 - 1 \right| \right) \tag{23}$$

A is determined by fitting equation (23) to the free energy curve constructed using the anhysteretic polarisation curve generated by the SMSM (Daniel et al., 2008). P_s is the saturation polarisation. It is obtained from the measured polarisation curve (maximum value of the P-E loop). The choice of the function (23) is based on the similarity between the shape of this function and the free energy curve obtained (François-Lavet et al., 2013).

The polarisation is calculated by minimisation of the functional $\Omega^k(E, \mathbf{P}^k, \mathbf{P}^k_{(p)})$. The next step is to identify κ^k and ω^k. The procedure of identification is developed in the next section.

The EB-Model is able to generate the macroscopic strain evolution by considering a quadratic polynomial function as expressed in equation (24).

$$S_{33} = Q \times {P_3}^2 \tag{24}$$

The coupling parameter Q is obtained by least squares regression over all points of the measured strain-polarisation loops (Fig. 13). It is recalled that (24) is only intended to describe the longitudinal strain under no applied stress. If a static stress was to be considered, the parameter Q shall then be identified for each considered stress state, taking the strain under no applied electric field as the reference (zero) strain.

3.4. Identification procedure

The identification procedure is performed on unpoled materials. There are different methods of depoling, with different effect on the material: A thermal method by applying a temperature above Curie temperature, an electrical method which consist of applying a decreasing cyclic electrical loading (Kaeswurm et al., 2018) or a mechanical depoling which is the application of a compressive stress on samples (Li et al., 2010). In this study, the electrical method is applied to depole the samples.

The next step after depolarisation of the samples is to apply a cyclic electrical loading with increasing amplitudes and record the variation of dielectric displacement to construct hysteresis loops (Fig. 6). The curves obtained will be used for identification procedure or validation. The method used for parameter identification was initially designed for ferromagnetic materials by Henrotte, then Jacques (Henrotte et al., 2006; Jacques et al., 2018). It is detailed hereafter. Later on, an analytical formula to identify Energy-Based parameters was developed by (Scorretti and Sixdenier, 2022).

Starting from an unpoled state where $E^*_{rev}(\lambda) = 0 \forall \lambda$, a unidirectional electric field is applied to the specimen from $E = 0$ up to $E = E_P$. The polarisation in each cell satisfies Equation (11), the dielectric state of cells is modified when $\kappa^*(\lambda) < E_A$, and one has for them, after loading, $E^*_{rev} = E_P - \kappa^*(\lambda)$.

The macroscopic reversible electric field is given by:

$$E_{rev}(0 \to E_P) = \int_0^\infty \omega(\kappa^*) \max(E_P - \kappa^*(\lambda), 0) d\kappa^* = F(E_P) \tag{25}$$

where $\omega(\kappa^*) = \frac{\zeta(\kappa^*/\kappa_{unit})}{\kappa_{unit}}$ is the equivalent of the probability density $\zeta(\lambda)$ but expressed as a function of κ^*. κ_{unit} is a constant factor expressed in unit of the electric field. $F(E)$ is the auxiliary function used in the procedure of identification, defined by:

$$F(E) = \int_0^E \omega(\kappa^*)(E - \kappa^*) d\kappa^* \tag{26}$$

For a given hysteresis loop, the coercive field $E_c(E)$ is characterized by:

$$P_{an}(E_{rev}(0 \to E \to -E_c(E))) = 0 \tag{27}$$

Which involves:

$$F(E) - 2F\left(\frac{E + E_c(E)}{2}\right) = 0 \tag{28}$$

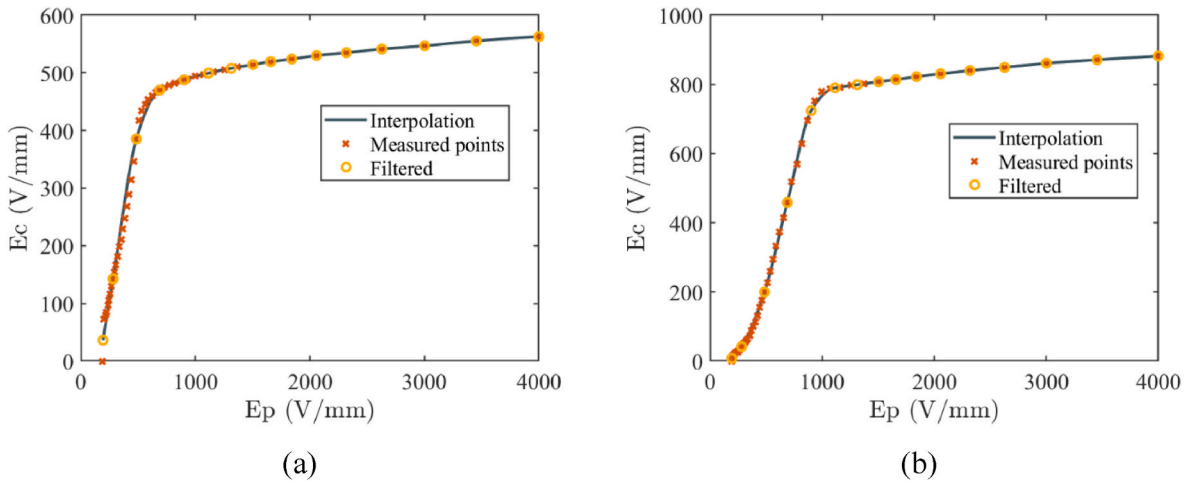

Fig. 7. Coercive field as a function of the electric field for (a) NCE55 and (b) PIC 153. Red points are representing the measured data, and the orange circles are the points that fit in the interpolation.

The coercive field can be obtained by applying a loading with increasing amplitudes and can be measured from the resulting hysteresis loops. The auxiliary function is constructed using the curve of E_c versus E_P (Fig. 6), and satisfies the criteria hereunder.

- $F(0) = 0$,
- $F(E) = E - E_{c,max} \forall E > E_{sat}$.

We define the sequence:

$$x^n = \frac{x^{n-1} + E_c(x^{n-1})}{2} < x^{n-1} \tag{29}$$

E_{sat} is the electric field at saturation. Starting from a certain value $x^0 > E_{sat}$ for which $F(x^0) = x^0 - E_{C,max}$, all the subsequent terms of the series are given by $F(x^n) = F(x^{n-1})/2$. This series is strictly decreasing and converges toward $F(0) = 0$.

The coercive field characteristic is interpolated linearly in the measurement range $[E_{min}, E_{max}]$ as follows:

$$\begin{cases} E_c(E) = E_{c,max} \text{ if } E > E_{max} \\ E_c(E) = E_{c,min}\left(\frac{E}{E_{min}}\right)^2 \text{ if } E < E_{min} \end{cases} \tag{30}$$

As it is a geometric progression, the values of the series appear to be equidistant in the logarithmic scale. If the auxiliary function is well interpolated and extrapolated, it shows a smoothness and a well-defined asymptotic behaviour.

$$\begin{cases} F(E) = E - E_{c,max} \text{ if } E > E_{max} \\ F(E) = \alpha E \text{ if } E < E_{max} \end{cases} \tag{31}$$

α is a material constant. The auxiliary function is constructed and drawn in Fig. 7, the reversible part is also drawn, and it corresponds to a straight line of a unitary slope since there is no coercive field by definition,

The auxiliary function is constructed and interpolated using Makima method. The resulting curve is smooth, which will allow us to calculate the values of the first and second derivatives of $F(E)$ using the finite difference method:

$$\partial_E F(x^j) = F(x^j)\frac{\Delta_2 - \Delta_1}{\Delta_1 \Delta_2} + F(x^{j+1})\frac{\Delta_1}{\Delta_2 \Delta_3} + F(x^{j-1})\frac{\Delta_2}{\Delta_1 \Delta_3}$$

$$\partial_E^2 F(x^j) = 2\left(\frac{F(x^{j-1})}{\Delta_1 \Delta_3} - \frac{F(x^j)}{\Delta_1 \Delta_2} + \frac{F(x^{j+1})}{\Delta_2 \Delta_3}\right)$$

$$\Delta_1 = x^j - x^{j-1}, \Delta_2 = x^{j+1} - x^j, \Delta_3 = x^{j+1} - x^{j-1}$$

Fig. 8 represents a spline interpolation of the first derivative of F using $\partial_E F(x^j)$, which represent the cumulative distribution function of the pinning field. $\partial_E F$ reaches a saturation value around $\kappa = 2000$ (V/

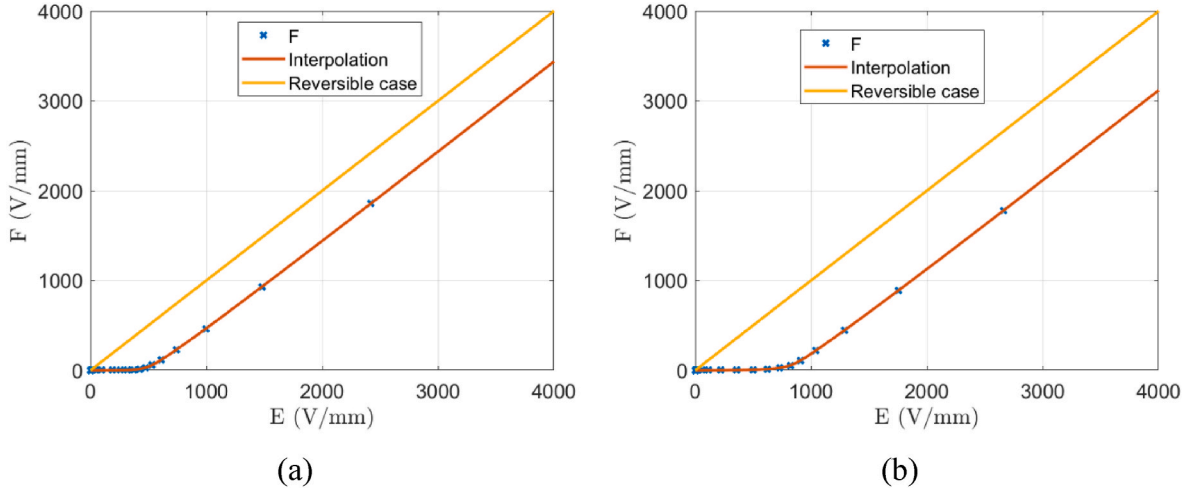

Fig. 8. Auxiliary function for (a) NCE55 and (b) PIC153.

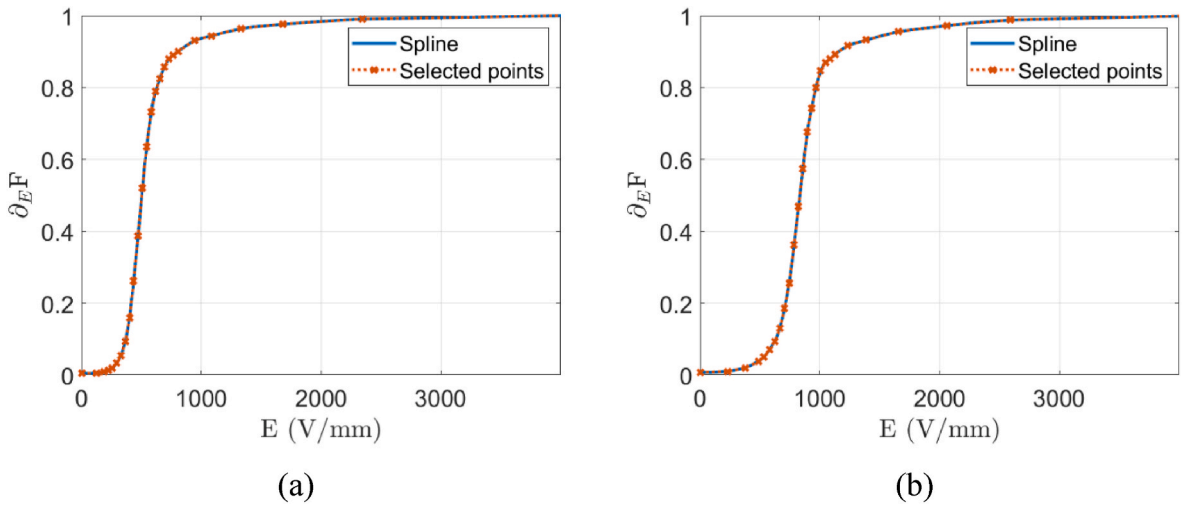

Fig. 9. Spline interpolation of the pinning field cumulative distribution function for (a) NCE55 and (b) PIC153.

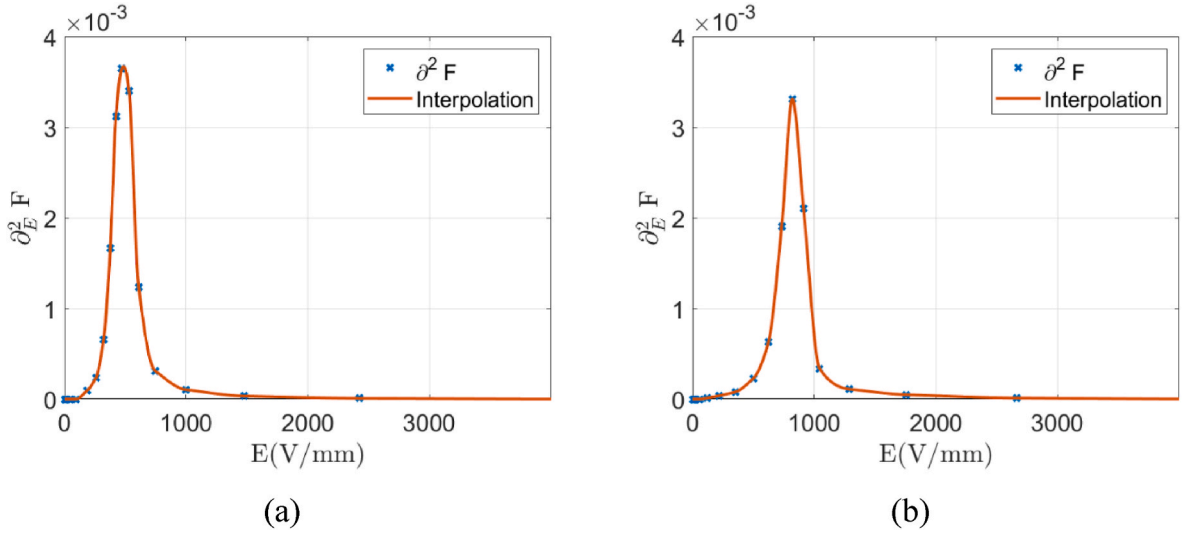

Fig. 10. Pinning field probability density for (a) NCE55 (b) PIC153.

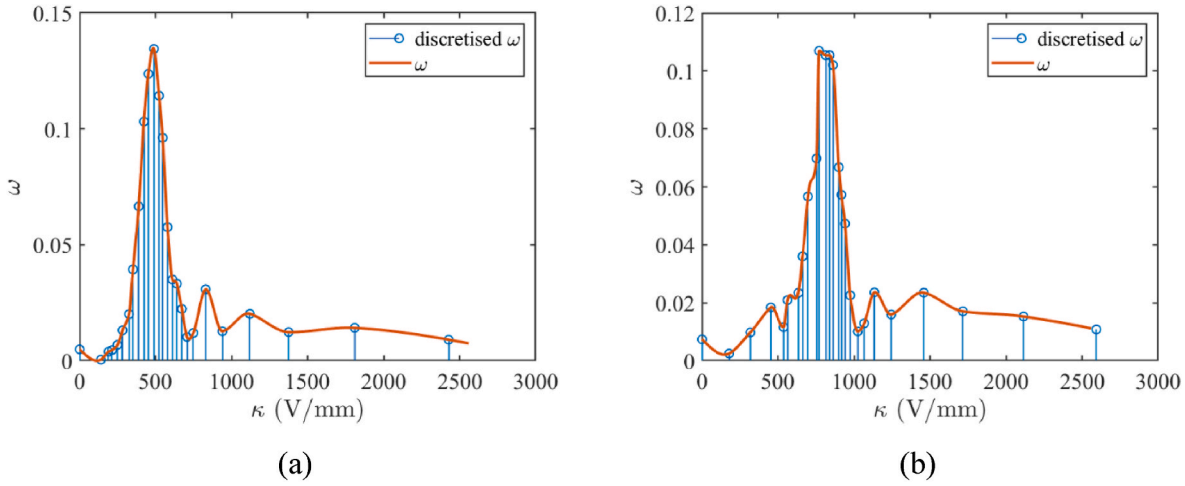

Fig. 11. Discretization of the pinning field probability density for (a) NCE55 and (b) PIC153.

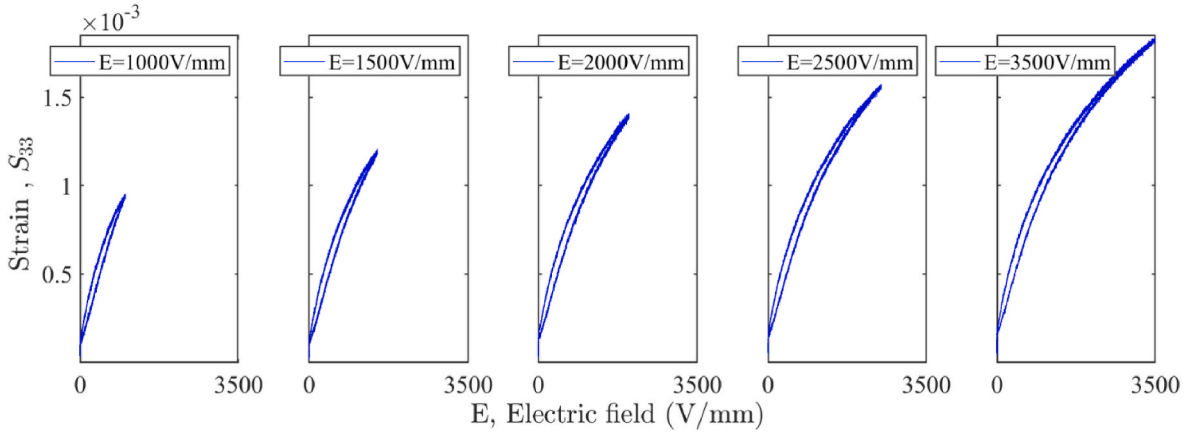

Fig. 12. Longitudinal strain S33 under increasing unipolar loading for a frequency of 50 mHz for PIC153.

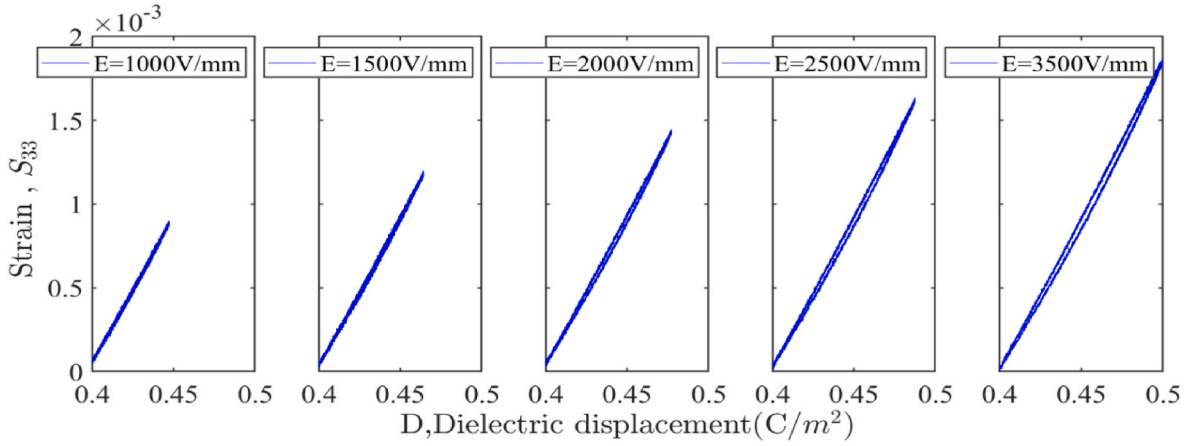

Fig. 13. Longitudinal strain as function of dielectric displacement for increasing unipolar loading of a frequency of 50 mHz for PIC153.

mm) for both materials.

The terms of the first derivative are used to calculate the second derivative of the auxiliary function which represents the pinning field probability density (Fig. 9). Fig. 10 shows pinning field probability density of κ^* after discretization in the cases of PIC153 and NCE55 samples, respectively. Each value of pinning field strength κ^* has its own corresponding probability (Fig. 11).

It is worth noting that the probability density (ω) has a non-zero value at $\kappa = 0$. Pinning field probability density gains its maximum value around the coercive field of the major loop obtained experimentally, and then by increasing κ value, it starts to decrease until zero.

For the numerical implementation, the continuous probability density $\omega(\kappa^*)$ is discretised. The pinning field is divided into N cells. Each cell is characterized by a pinning field κ^k and its weight ω^k. For this purpose, a linear piecewise function $y(x)$ is considered.

The number of points x^k is fixed a priori. An optimization process is applied to define the best partitioning of the electric field and the positions of (x^k, y^k). The parameters κ^k and ω^k are calculated using the coordinates (x^k, y^k).

The numerical values for the material parameters used in this study are given in Table 2.

Table 2
Material parameters for the proposed energy-based model.

Parameter	Description	Value for PIC 153	Value for NCE55	
A_s	Adjustment parameter	3.1×10^{-5} m^3/J	1.5×10^{-5} m^3/J	SMSM Equation (22) and (Daniel et al., 2014b)
P_0	Spontaneous polarisation	0.41 C.m^{-2}	0.40 C.m^{-2}	
ε	Dielectric permittivity	0.02 μF.m^{-1}	0.02 μF.m^{-1}	
A	Free energy parameter	3.55×10^5 C.m^{-1}.V^{-1}	2.7×10^5 C.m^{-1}.V^{-1}	Free energy Equation (23)
P_s	Saturation polarisation	0.34 C.m^{-2}	0.33 C.m^{-2}	
Q	Coupling parameter	3.7×10^{-3}m^2.C^{-1}	3.32×10^{-3}m^2.C^{-1}	Strain Equation (24)
ω^k	Weight of pinning field	See section 3.4.		Dissipation function
κ^k	Pinning field strength	See section 3.4.		
N	Number of cells	26		

4. Validation

To highlight the capability of the energy-based model for the description of the ferroelectric behaviour, first, a comparison between the experimental data and a symmetrical hysteresis major loop is illustrated. Then, a second comparison is realised between the loop generated by the model and the experimental result for a unipolar loading for different amplitudes. The results used for model validation are different from the experimental curves used for identification.

In Fig. 14, a major hysteresis loop is presented, for both PIC153 and NCE55, where a good agreement between the experimental curve and

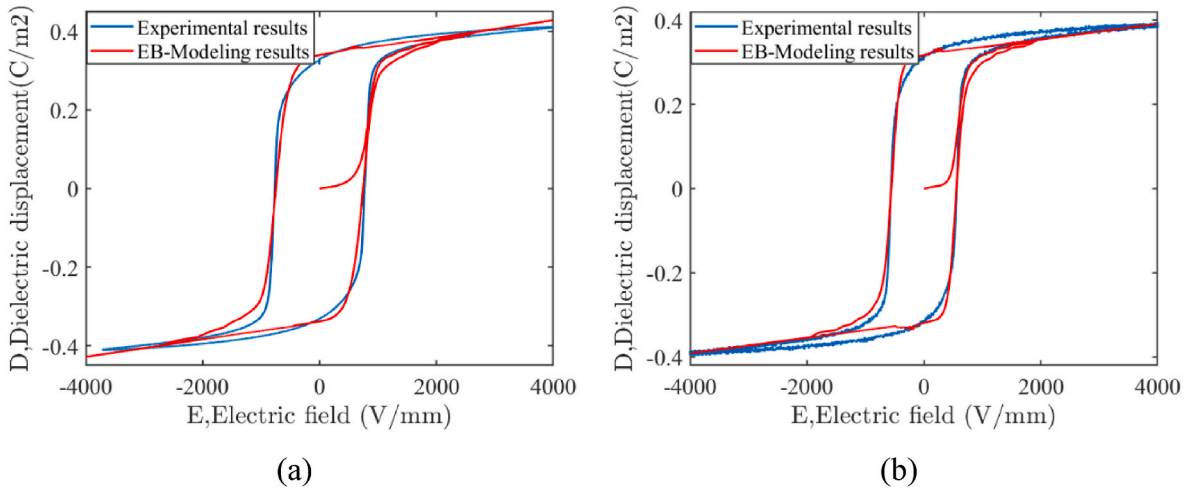

Fig. 14. Major hysteresis loop for (a) PIC153 and (b) NCE55.

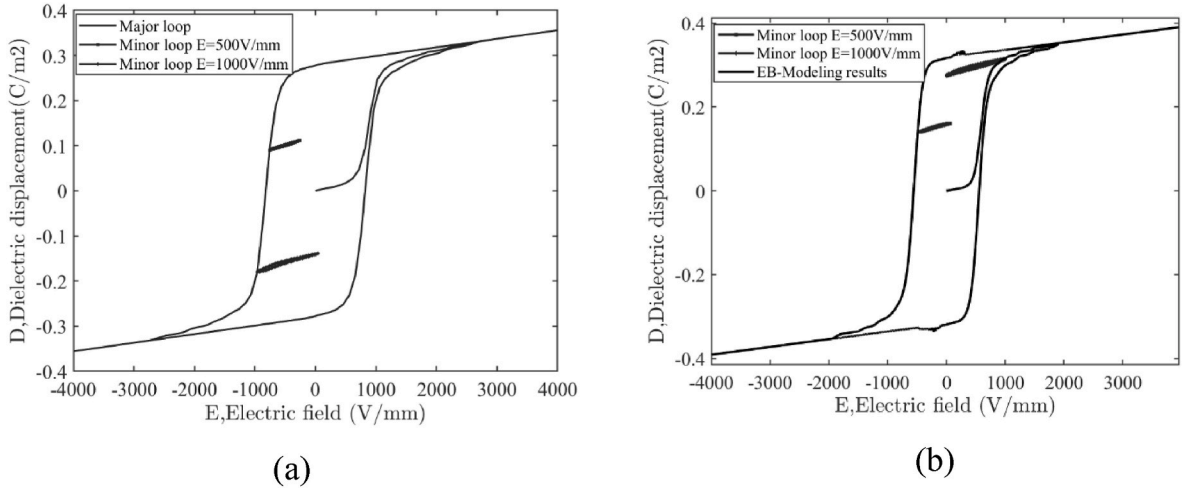

Fig. 15. Major hysteresis loop with inner loops for (a) PIC153 and (b) NCE55.

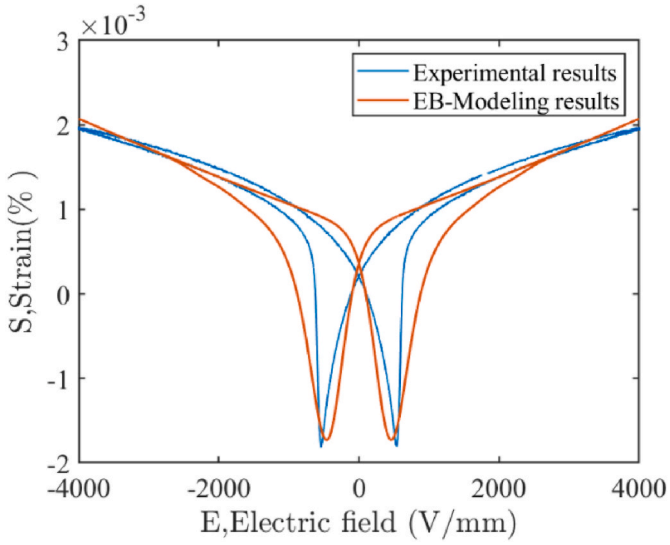

Fig. 16. Major strain curve loops for NCE55.

the EB-Model results can be seen. Fig. 15 shows the capability of the model to generate internal minor loops. Using equation (24), strain loops can also be obtained as shown in Fig. 16. A comparison is made between the experimental strain loop and the modelling results. The observed differences can be explained by the strong assumptions made in the definition of the strain-polarisation relationship: polynomial restricted to the order two and use of a one-to-one function while experimental measurements show some hysteresis in strain-polarisation response.

To test the accuracy of this model, and to correlate it with the way ferroelectrics are used in most practical applications, the D(E) and S(E) loops for unipolar loading on PIC 153 and NCE55 are illustrated in Figs. 17–19 and Fig. 20. The experimental results describe the behaviour of the material close to saturation state. Therefore, all cycles are narrow compared to bipolar cycles. The model is able to capture the behaviour for this case of loading as seen in the figures below. The comparison shows that both loops have the same shape, even the same area, with a tiny difference in the behaviour towards saturation. The difference might be caused by the variation of the piezoelectric coefficient which is dependant to the electric field amplitude. The results presented in Figs. 19 and 20 show the strain loop generated by the model in comparison to the measurements obtained by the laser sensor.

The experimental dissipated energy (i.e., the area of the dielectric displacement-electric field hysteresis cycle) is obtained and compared to

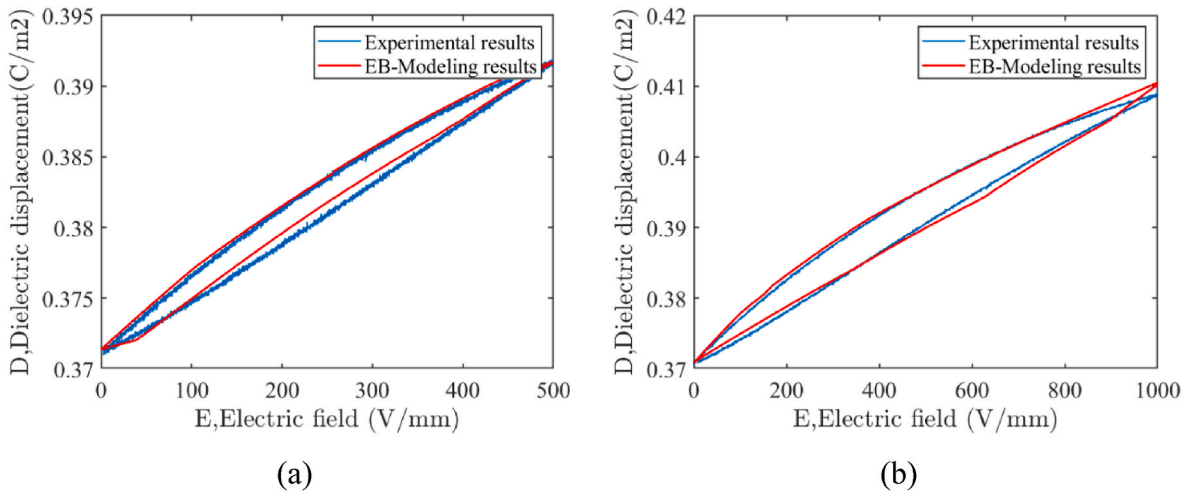

Fig. 17. Minor hysteresis loops for a unipolar electric field, around remnent polarisation for PIC153 for an amplitude of (a) E = 500 (V/mm) and (b) E = 1000 (V/mm).

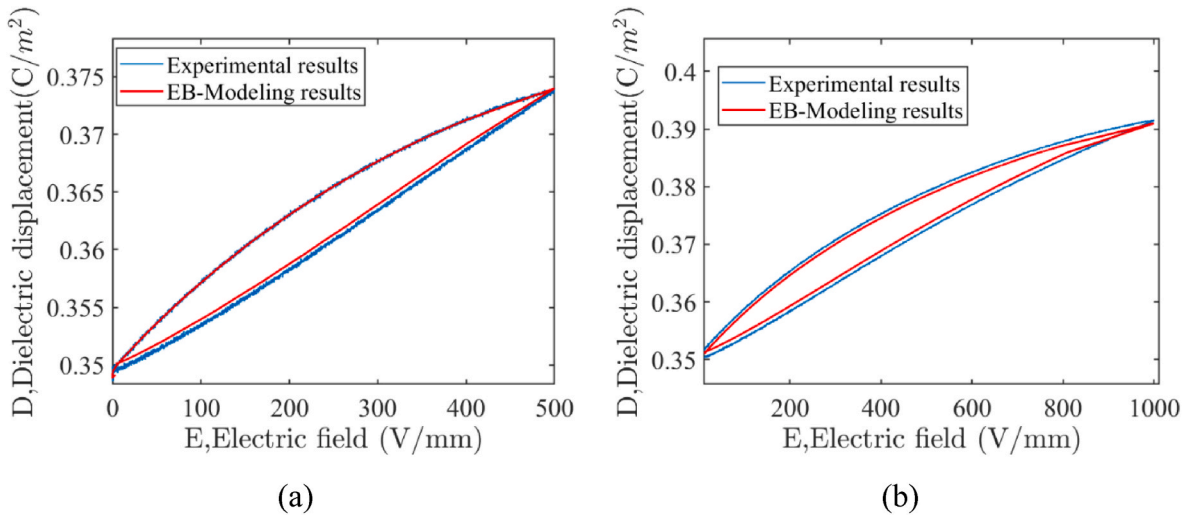

Fig. 18. Minor hysteresis loops for a unipolar electric field, around remnent polarisation for NCE55 for an amplitude of (a) E = 500 (V/mm) and (b) E = 1000 (V/mm).

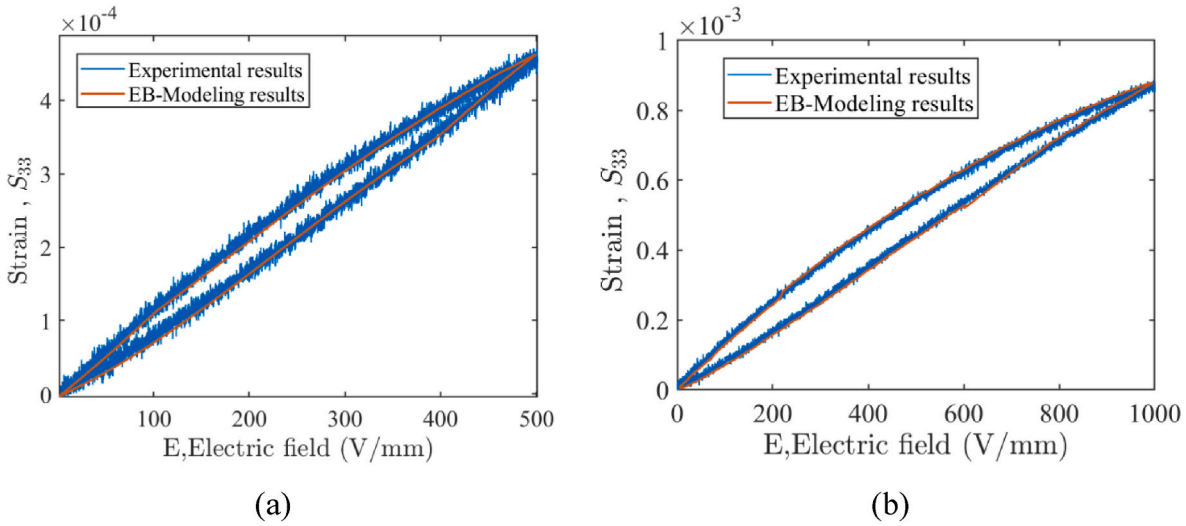

Fig. 19. Strain loops for a unipolar loading on PIC 153, (a) E = 500 (V/mm) (b) E = 1000 (V/mm).

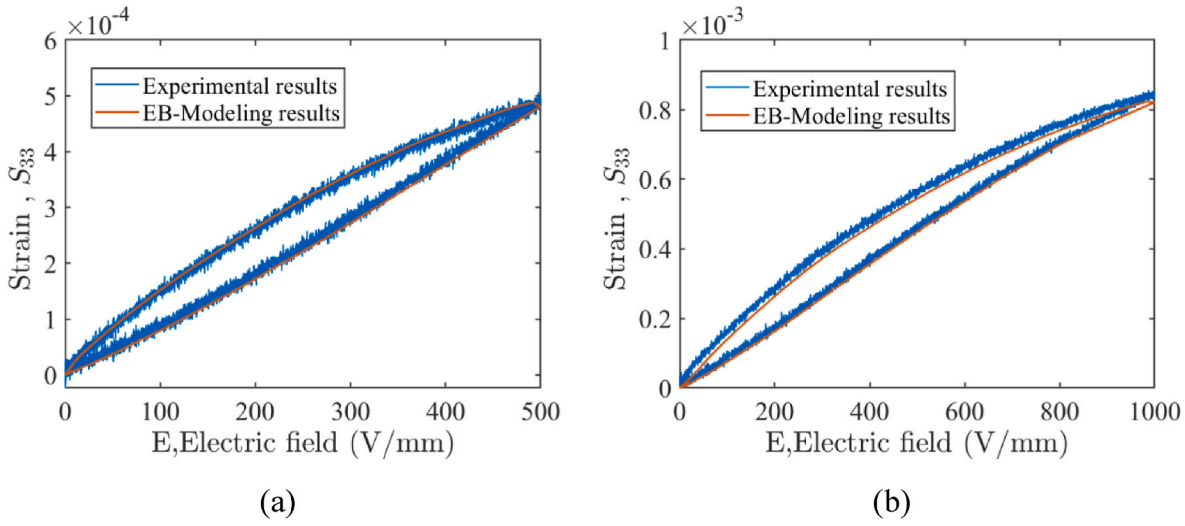

Fig. 20. Strain loops for a unipolar loading on NCE55, (a) E = 500 (V/mm) (b) 1000 (V/mm).

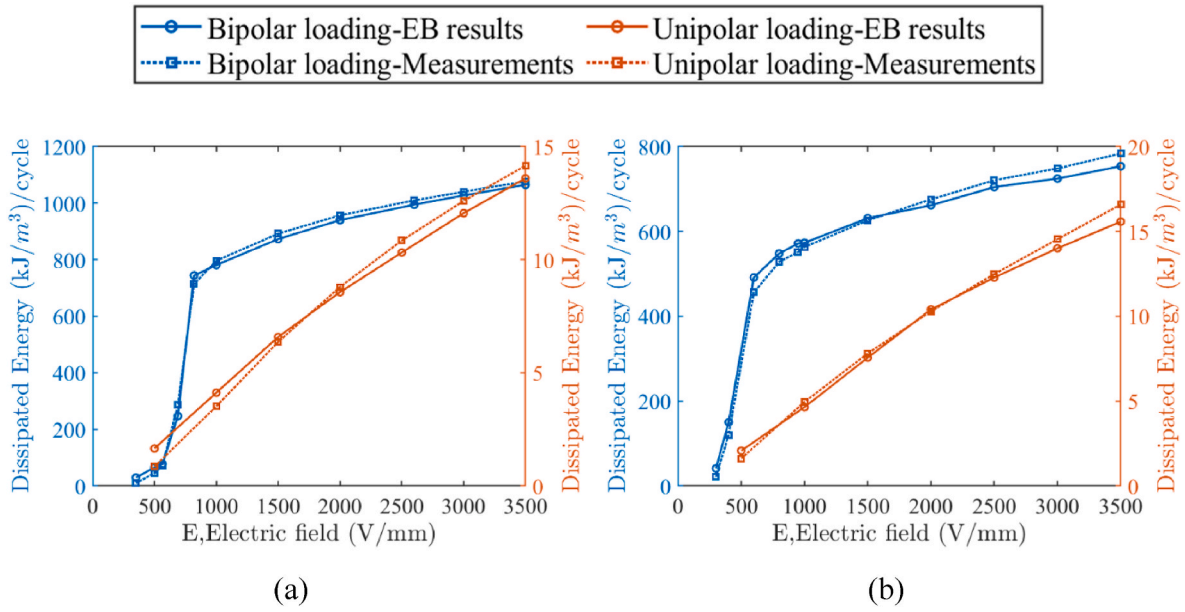

Fig. 21. Dissipated energy evolution for (a) PIC153 and (b) NCE55 under bipolar and unipolar growing electric field.

the calculated dissipation generated by the energy-based model (Fig. 21). This comparison shows good agreement between the experimental and modelling results, especially around the coercive field for the bipolar load where the dissipation increases rapidly. The saturation of the dissipated energy around 3500V/mm under bipolar loading is also captured by the model. Such a good agreement between experiments and modelling is very promising for the study of functional fatigue in ferroelectrics, for which the cumulative dissipated energy is a key aspect.

5. Conclusion

An energy-based model to describe the behaviour of ferroelectric ceramics is proposed in this paper. The model relies on two constitutive functions: The free energy and the dissipation. The dissipation is generated by the pinning of the walls while the free energy is defined using a simplified formulation of a multi-scale model. To give more accuracy to the model, a multi-cell approach is adopted to characterize the different and rapidly varying strengths of pinning fields at the microscopic scale.

For the numerical implementation, a variational approach was adopted, and it consists of solving the fundamental equation of the energy-based model and calculate the polarisation at each iteration. For each cell, a functional of polarisation $\Omega(\mathbf{P})$ is assigned, then minimized to calculate the polarisation $\mathbf{P}^*$ .To minimize the functional $\Omega(\mathbf{P})$, the strength of the pinning field κ and the pinning field probability density ω has to be identified. In the identification procedure, an electrically unpoled sample was used. The procedure consists of applying a cyclic electric field with increasing amplitudes, extracting the coercive field E_c from the hysteresis loops and constructing an auxiliary function F which is used to calculate the pinning field intensity and its corresponding probability density. The performance of the model is shown for different types of loading, and the comparison between experimental and modelling results is presented in the validation section. The model is tested under unipolar loading around remnant polarisation, which is the most common case in practical applications, and it shows its ability to describe the polarisation and strain evolution for the two materials used in the experiments. The dissipated energy for PIC153 and NCE55 under

unipolar and bipolar loading is calculated using the energy-based model and is compared to the measurements. These results can be used to define the operating range to be selected according to the application. The model is also a promising tool to study functional fatigue of ferroelectrics, due to its sound thermodynamic consistency.

A natural extension for the energy-based model would involve describing the behaviour under more complex loading configurations. This includes simultaneous electric and mechanical loadings, multiaxial electric field loadings or cycling loadings. Such extensions will be built by taking full advantage of the multi-scale model formulation for the anhysteretic behaviour.

Efforts are underway to improve the model and address this limitation. Future works also aim to enhance the model by incorporating more significant internal variables, including strain. Additionally, the implementation of the energy-based model in a finite element code will enable the evaluation of multiaxial loading cases and facilitate field studies on heterogeneous specimens.

Author statement

Chaimae Babori: Conceptualization, Methodology, Software, Investigation, Validation, Visualization, Writing - Original Draft; **Mahmoud Barati:** Conceptualization, Methodology, Investigation, Validation, Supervision, Writing - Review & Editing; **Laurent Daniel:** Conceptualization, Validation, Supervision, Project administration, Funding acquisition, Writing - Review & Editing.

Declaration of competing interest

All the authors declare that they have no potential conflicts of interest regarding publication of this article.

Data availability

Data will be made available on request.

Acknowledgments

The authors wish to acknowledge CentraleSupelec for their financial and material support to this Research.

References

Arockiarajan, A., Sivakumar, S.M., Sansour, C., 2010. A thermodynamically motivated model for ferroelectric ceramics with grain boundary effects. Smart Mater. Struct. 19 https://doi.org/10.1088/0964-1726/19/1/015008.

Barati, M., Amini, B., Segouin, V., Daniel, L., Chirani, S.A., Calloch, S., 2021. Investigation of self-heating and dissipative effects in ferroelectric ceramics subjected to compressive mechanical cyclic loading. Acta Mater. 221, 117386 https://doi.org/10.1016/j.actamat.2021.117386.

Bassiouny, E., Ghaleb, A.F., Maugin, G.A., 1988a. Thermodynamical formulation for coupled electromechanical hysteresis effects—I. Basic equations. Int. J. Eng. Sci. 26, 1279–1295. https://doi.org/10.1016/0020-7225(88)90047-X.

Bassiouny, E., Ghaleb, A.F., Maugin, G.A., 1988b. Thermodynamical formulation for coupled electromechanical hysteresis effects-II. Poling of ceramics. Int. J. Eng. Sci. 26, 1297–1306. https://doi.org/10.1016/0020-7225(88)90048-1.

Bassiouny, E., Maugin, G.A., 1989a. Thermodynamical formulation for coupled electromechanical hysteresis effects—IV. Combined electromechanical loading. Int. J. Eng. Sci. 27, 989–1000. https://doi.org/10.1016/0020-7225(89)90039-6.

Bassiouny, E., Maugin, G.A., 1989b. Thermodynamical formulation for coupled electromechanical hysteresis effects-III. Parameter identification. Int. J. Eng. Sci. 27, 975–987. https://doi.org/10.1016/0020-7225(89)90038-4.

Bergqvist, A., 1997. Magnetic vector hysteresis model with dry friction-like pinning. Phys. B Condens. Matter 233, 342–347. https://doi.org/10.1016/S0921-4526(97)00319-0.

Bergqvist, A., Lundgren, A., Engdahl, G., 1997. Experimental testing of an anisotropic vector hysteresis model. IEEE Trans. Magn. 33, 4152–4154. https://doi.org/10.1109/20.619693.

Bertotti, G., 1998. Hysteresis in Magnetism: for Physicists, Materials Scientists, and Engineers. Gulf Professional Publishing.

Booth, R., Goldsmith, P., 2017. Detecting finger gestures with a wrist worn piezoelectric sensor array. In: 2017 IEEE International Conference on Systems, Man, and Cybernetics. SMC 2017, pp. 3665–3670. https://doi.org/10.1109/SMC.2017.8123202.

Cao, H., Evans, A.G., 1993. Nonlinear deformation of ferroelectric ceramics. J. Am. Ceram. Soc. 76, 890–896. https://doi.org/10.1111/j.1151-2916.1993.tb05312.x.

Chen, P.J., 1980. Three dimensional dynamic electromechanical constitutive relations for ferroelectric materials. Int. J. Solid Struct. 16, 1059–1067. https://doi.org/10.1016/0020-7683(80)90063-3.

Cocks, A.C.F., Mcmeeking, R.M., Cocksa, A.C.F., Mcmeeking, R.M., 1999. A Phenomenological Constitutive Law for the Behaviour of Ferroelectric Ceramics, vol. 228, pp. 219–228. https://doi.org/10.1080/00150199908226136.

Da Silva, L.G., Abderahmane, A., Domenjoud, M., Bernard, L., Daniel, L., 2022. An extension of the vector-play model to the case of magneto-elastic loadings. IEEE Access. https://doi.org/10.1109/ACCESS.2022.3222833.

Damjanovic, D., 2001. Ferroelectric sensors. IEEE Sensor. J. 1, 191–206. https://doi.org/10.1109/JSEN.2001.954832.

Damjanovic, D., Taylor, D.V., 1999. Contributions to the nonlinear dielectric and piezoelectric response of ferroelectric thin films and ceramics. Ferroelectrics 221, 137–146. https://doi.org/10.1080/00150199908016448.

Daniel, L., Hall, D.A., Koruza, J., Webber, K.G., King, A., Withers, P.J., 2015. Revisiting the blocking force test on ferroelectric ceramics using high energy x-ray diffraction. J. Appl. Phys. 117, 174104 https://doi.org/10.1063/1.4918928.

Daniel, L., Hall, D.A., Withers, P.J., 2014a. A multiscale modelling analysis of the contribution of crystalline elastic anisotropy to intergranular stresses in ferroelectric materials. J. Phys. D Appl. Phys. 47, 8. https://doi.org/10.1088/0022-3727/47/32/325303.

Daniel, L., Hall, D.A., Withers, P.J., 2014b. A multiscale model for reversible ferroelectric behaviour of polycrystalline ceramics. Mech. Mater. 71, 85–100. https://doi.org/10.1016/j.mechmat.2014.01.006.

Daniel, L., Hubert, O., Buiron, N., Billardon, R., 2008. Reversible magneto-elastic behavior: a multiscale approach. J. Mech. Phys. Solid. 56, 1018–1042. https://doi.org/10.1016/j.jmps.2007.06.003.

François-Lavet, V., Henrotte, F., Stainier, L., Noels, L., Geuzaine, C., 2013. An energy-based variational model of ferromagnetic hysteresis for finite element computations. J. Comput. Appl. Math. 246, 243–250. https://doi.org/10.1016/j.cam.2012.06.007.

Glazer, A.M., Groves, P., Smith, D.T., 1984. Automatic sampling circuit for ferroelectric hysteresis loops. J. Phys. Educ. 17, 95–97. https://doi.org/10.1088/0022-3735/17/2/001.

Granzow, T., Glinsek, S., Defay, E., 2021. Piezoelectric ceramics. In: Encyclopedia of Smart Materials. Elsevier, pp. 22–34. https://doi.org/10.1016/B978-0-12-815732-9.00043-7.

Guillon, O., Delobelle, P., Thiébaud, F., Walter, V., Perreux, D., 2004. Uniaxial electromechanical behavior of a soft PZT: experiments and modeling. Ferroelectrics 308, 95–111. https://doi.org/10.1080/00150190490508882.

Henrotte, F., Nicolet, A., Hameyer, K., 2006. An energy-based vector hysteresis model for ferromagnetic materials. COMPEL - Int. J. Comput. Math. Electr. Electron. Eng. 25, 71–80. https://doi.org/10.1108/03321640610634344.

Henrotte, F., Steentjes, S., Hameyer, K., Geuzaine, C., 2014. Iron loss calculation in steel laminations at high frequencies. IEEE Trans. Magn. 50, 333–336. https://doi.org/10.1109/TMAG.2013.2282830.

Hill, R., 1966. Generalized constitutive relations for incremental deformation of metal crystals by multislip. J. Mech. Phys. Solid. 14, 95–102. https://doi.org/10.1016/0022-5096(66)90040-8.

Huber, J.E., 2005. Micromechanical modelling of ferroelectrics. Curr. Opin. Solid State Mater. Sci. 9, 100–106. https://doi.org/10.1016/j.cossms.2006.05.001.

Huber, J.E., Fleck, N.A., Landis, C.M., McMeeking, R.M., 1999. Constitutive model for ferroelectric polycrystals. J. Mech. Phys. Solid. 47, 1663–1697. https://doi.org/10.1016/S0022-5096(98)00122-7.

Hwang, S.C., Lynch, C.S., McMeeking, R.M., 1995. Ferroelectric/ferroelastic interactions and a polarization switching model. Acta Metall. Mater. 43, 2073–2084. https://doi.org/10.1016/0956-7151(94)00379-V.

Jacques, K., 2018. Energy-Based Magnetic Hysteresis Models - Theoretical Development and Finite Element Formulations, vol. 254.

Jacques, K., Steentjes, S., Henrotte, F., Geuzaine, C., Hameyer, K., 2018. Representation of microstructural features and magnetic anisotropy of electrical steels in an energy-based vector hysteresis model. AIP Adv. 8 https://doi.org/10.1063/1.4994199.

Kaeswurm, B., Segouin, V., Daniel, L., Webber, K.G., 2018. The anhysteretic polarisation of ferroelectrics. J. Phys. D Appl. Phys. 51 https://doi.org/10.1088/1361-6463/aaa698.

Kamlah, M., 2001. Ferroelectric and ferroelastic piezoceramics - modeling of electromechanical hysteresis phenomena. Continuum Mech. Therm. https://doi.org/10.1007/s001610100052.

Kamlah, M., Böhle, U., 2001. Finite element analysis of piezoceramic components taking into account ferroelectric hysteresis behavior. Int. J. Solid Struct. 38, 605–633. https://doi.org/10.1016/S0020-7683(00)00055-X.

Kamlah, M., Tsakmakis, C., 1999. Phenomenological modeling of the non-linear electromechanical coupling in ferroelectrics. Int. J. Solid Struct. 36, 669–695. https://doi.org/10.1016/S0020-7683(98)00040-7.

Kamlah, M., Wang, Z., 2003. A thermodynamically and microscopically motivated constitutive model for piezoceramics. Comput. Mater. Sci. 28, 409–418. https://doi.org/10.1016/j.commatsci.2003.08.002.

Kimura, M., Ando, A., Sakabe, Y., 2010. Lead zirconate titanate-based piezo-ceramics. In: Advanced Piezoelectric Materials: Science and Technology. Woodhead Publishing, pp. 89–110. https://doi.org/10.1533/9781845699758.1.89.

Landis, C.M., 2002. Fully coupled, multi-axial, symmetric constitutive laws for polycrystalline ferroelectric ceramics. J. Mech. Phys. Solid. 50, 127–152. https://doi.org/10.1016/S0022-5096(01)00021-7.

Landis, C.M., McMeeking, R.M., 1999. A phenomenological constitutive law for ferroelastic switching and a resulting asymptotic crack tip solution. J. Intell. Mater. Syst. Struct. 10, 155–163. https://doi.org/10.1177/1045389x9901000209.
Lange, S., Ricoeur, A., 2015. A condensed microelectromechanical approach for modeling tetragonal ferroelectrics. Int. J. Solid Struct. 54, 100–110. https://doi.org/10.1016/j.ijsolstr.2014.11.004.
Li, F.X., Rajapakse, R.K.N.D., 2007. Analytical saturated domain orientation textures and electromechanical properties of ferroelectric ceramics due to electric/mechanical poling. J. Appl. Phys. 101, 54110 https://doi.org/10.1063/1.2645889.
Li, J.Y., Rogan, R.C., Üstündag, E., Bhattacharya, K., 2005. Domain switching in polycrystalline ferroelectric ceramics. Nat. Mater. 4, 776–781. https://doi.org/10.1038/nmat1485.
Li, Y.W., Zhou, X.L., Li, F.X., 2010. Temperature-dependent mechanical depolarization of ferroelectric ceramics. J. Phys. D Appl. Phys. 43, 175501 https://doi.org/10.1088/0022-3727/43/17/175501.
Lobanov, S.M., Semenov, A.S., 2019. Finite-element modeling of ferroelectric material behavior at morphotropic phase boundaries between tetragonal, rhombohedric and orthorhombic phases. In: Journal of Physics: Conference Series, 012062. https://doi.org/10.1088/1742-6596/1236/1/012062.
Lynch, C.S., 1996. The effect of uniaxial stress on the electro-mechanical response of 8/65/35 PLZT. Acta Mater. 44, 4137–4148. https://doi.org/10.1016/S1359-6454(96)00062-6.
Mahbub, I., Pullano, S.A., Wang, H., Islam, S.K., Fiorillo, A.S., To, G., Mahfouz, M.R., 2017. A low-power wireless piezoelectric sensor-based respiration monitoring system realized in CMOS process. IEEE Sensor. J. 17, 1858–1864. https://doi.org/10.1109/JSEN.2017.2651073.
McMeeking, R.M., Landis, C.M., 2002. A phenomenological multi-axial constitutive law for switching in polycrystalline ferroelectric ceramics. Int. J. Eng. Sci. 40, 1553–1577. https://doi.org/10.1016/S0020-7225(02)00033-2.
Meindlhumer, M., Pechstein, A., Humer, A., 2021. Variational inequalities for ferroelectric constitutive modeling. J. Intell. Mater. Syst. Struct. 32, 317–330. https://doi.org/10.1177/1045389X20951252.
Miehe, C., Rosato, D., Kiefer, B., 2011. Variational principles in dissipative electro-magneto-mechanics: a framework for the macro-modeling of functional materials. Int. J. Numer. Methods Eng. 86, 1225–1276. https://doi.org/10.1002/nme.3127.
Mielke, A., Timofte, A.M., 2006. An energetic material model for time-dependent ferroelectric behaviour: existence and uniqueness. Math. Methods Appl. Sci. 29, 1393–1410. https://doi.org/10.1002/mma.731.
Noliac, 2022. Noliac Piezoceramic Material NCE51 - Noliac - Your Piezo Partner [WWW Document]. Noliac. URL. http://www.noliac.com/products/materials/nce55/. (Accessed 28 September 2022).
Pardo, L., Ricote, J., 2011. Multifunctional Polycrystalline Ferroelectric Materials, vol. 140. Springer Series in Materials Science. https://doi.org/10.1007/978-90-481-2875-4.
Paruch, P., Guyonnet, J., 2013. Nanoscale studies of ferroelectric domain walls as pinned elastic interfaces. Compt. Rendus Phys. https://doi.org/10.1016/j.crhy.2013.08.004.
Pechstein, A.S., Meindlhumer, M., Humer, A., 2021. High-order mixed finite elements for an energy-based model of the polarization process in ferroelectric materials. J. Intell. Mater. Syst. Struct. 32, 355–368. https://doi.org/10.1177/1045389X20953895.
Pechstein, A.S., Meindlhumer, M., Humer, A., 2020. The polarization process of ferroelectric materials in the framework of variational inequalities. ZAMM Zeitschrift fur Angew. Math. und Mech. 100, e201900329 https://doi.org/10.1002/zamm.201900329.
PI Ceramic - Ceramic plates and blocks dimensions. [Online]. Available: https://www.piceramic.com/-%20en/products/piezoceramic-components/plates-and-blocks/.
Ricinschi, D., Okuyama, M., 2007. Field-dependent switching kinetics and ferroelectric hysteresis loops analyzed with a phenomenological model in relation to typical experiments. In: Ferroelectrics. Taylor & Francis Group, pp. 111–127. https://doi.org/10.1080/00150190701260918.
Sands, C.M., Guz, I.A., 2013. Unidimensional model of polarisation changes in piezoelectric ceramics based on the principle of maximum entropy production. J. Eng. Math. 78, 249–259. https://doi.org/10.1007/s10665-011-9491-3.
Sateesh, V.L., Upadhyay, C.S., Venkatesan, C., 2008. Thermodynamic modeling of hysteresis effects in piezoceramics for application to smart structures. AIAA J. 46, 280–284. https://doi.org/10.2514/1.31885.
Schröder, J., Romanowski, H., 2005. A thermodynamically consistent mesoscopic model for transversely isotropic ferroelectric ceramics in a coordinate-invariant setting. In: Archive of Applied Mechanics, pp. 863–877. https://doi.org/10.1007/s00419-005-0412-7.
Scorretti, R., Sixdenier, F., 2022. An analytical formula to identify the parameters of the energy-based hysteresis model. J. Magn. Magn Mater. 548, 168748 https://doi.org/10.1016/j.jmmm.2021.168748.
Segouin, V., Domenjoud, M., Bernard, Y., Daniel, L., 2019. Mechanics-aided digital image correlation for the investigation of piezoelectric and ferroelectric behaviour of a soft PZT. J. Eur. Ceram. Soc. 39, 2091–2102. https://doi.org/10.1016/j.jeurceramsoc.2018.12.058.
Segouin, V., Domenjoud, M., Bernard, Y., Daniel, L., 2017. Development of a 2D DIC experimental tool for piezoelectric strains measurements. In: Conference Proceedings of the Society for Experimental Mechanics Series. Springer, Cham, pp. 45–50. https://doi.org/10.1007/978-3-319-51439-0_11.
Smith, R.C., 2005. Smart Material Systems, Smart Material Systems. Society for Industrial and Applied Mathematics (SIAM, 3600 Market Street, Floor, vol. 6, 19104. https://doi.org/10.1137/1.9780898717471. Philadelphia, PA.
Smith, R.C., Hom, C.L., 1999. Domain wall theory for ferroelectric hysteresis. J. Intell. Mater. Syst. Struct. 10, 195–213. https://doi.org/10.1177/1045389X9901000302.
Steentjes, S., Henrotte, F., Geuzaine, C., Hameyer, K., 2014. A dynamical energy-based hysteresis model for iron loss calculation in laminated cores. In: International Journal of Numerical Modelling: Electronic Networks, Devices and Fields. John Wiley and Sons Ltd, pp. 433–443. https://doi.org/10.1002/jnm.1931.
Su, Y., Weng, G.J., 2006. A polycrystal hysteresis model for ferroelectric ceramics. Proc. R. Soc. A Math. Phys. Eng. Sci. 462, 1573–1592. https://doi.org/10.1098/rspa.2005.1616.
Tan, W.L., Kochmann, D.M., 2017. An effective constitutive model for polycrystalline ferroelectric ceramics: theoretical framework and numerical examples. Comput. Mater. Sci. 136, 223–237. https://doi.org/10.1016/j.commatsci.2017.04.032.
Tomičević, Z., Hild, F., Roux, S., 2013. Mechanics-aided digital image correlation. J. Strain Anal. Eng. Des. 48, 330–343. https://doi.org/10.1177/0309324713482457.
Wang, D., Wang, L., Melnik, R., 2017. A hysteresis model for ferroelectric ceramics with mechanism for minor loops. Phys. Lett. Sect. A Gen. At. Solid State Phys. 381, 344–350. https://doi.org/10.1016/j.physleta.2016.11.013.
Yang, T.J., Gopalan, V., Swart, P.J., Mohideen, U., 1999. Direct observation of pinning and bowing of a single ferroelectric domain wall. Phys. Rev. Lett. 82, 4106–4109. https://doi.org/10.1103/PhysRevLett.82.4106.
Zhang, Q.M., Wang, H., Kim, N., Cross, L.E., 1994. Direct evaluation of domain-wall and intrinsic contributions to the dielectric and piezoelectric response and their temperature dependence on lead zirconate-titanate ceramics. J. Appl. Phys. https://doi.org/10.1063/1.355874.

Glossary

$\boldsymbol{D}$: Dielectric displacement
d_{33}, d_{31}: Piezoelectric coefficients
$\boldsymbol{E}$: Electric field
E_c: Coercive field
$\mathbf{E}_{irr}$: Irreversible electric field
$\mathbf{E}_{rev}$: Reversible electric field
E_{sat}: Saturation electric field
$\boldsymbol{P}$: Polarisation
P_{sat}: Saturation polarisation
$\boldsymbol{T}$: Stress
Δ: Dissipation
ε_{33}: Dielectric coefficients
κ: Pinning field intensity
ψ: Helmoltz Free energy
ω: Pinning field probability